Bootstrap Embedding For Large Molecular Systems

Hong-Zhou Ye, Henry K. Tran, and Troy Van Voorhis*

Department of Chemistry, Massachusetts Institute of Technology, Cambridge, MA 02139

E-mail: tvan@mit.edu

Abstract

Recent developments in quantum embedding theories have provided attractive approaches to correlated calculations for large systems. In this work, we extend our previous work [*J. Chem. Theory Comput.* 2019, **15**, 4497 – 4506; *J. Phys. Chem. Lett.* 2019, **10**, 6368 – 6374] on Bootstrap Embedding (BE) to enable correlated *ab initio* calculations at the coupled cluster with singles and doubles (CCSD) level for large molecules. We introduce several new algorithmic developments that significantly reduce the computational cost of BE, while maintaining its accuracy. The resulting implementation scales as $O(N^3)$ for the integral transform and $O(N)$ for the CCSD calculation. Numerical results on a series of conjugated molecules suggest that BE with reasonably sized fragments can recover more than 99.5% of the total correlation energy of a full CCSD calculation, while the required computational resources (time and storage) compare favorably to one popular local correlation scheme, domain localized pair natural orbital (DLPNO). The largest BE calculation in this work involves ~ 2900 basis functions and can be performed on a single node with 16 CPU cores and 64 GB of memory in a few days. We anticipate these developments represent an important step towards the application of BE to solve practical problems.

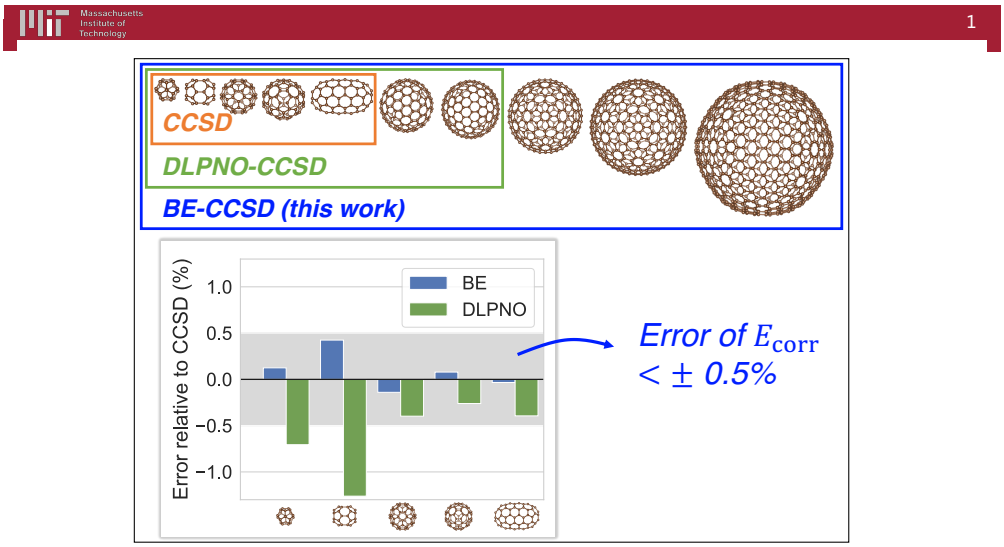

1 Introduction

Accurately modelling the electronic structure of chemical systems is crucial to understanding the atomistic mechanisms of many functional materials and designing new ones.[1–5] Achieving this goal from first principles requires correlated calculations that can capture the electron correlation missing at the Hartree-Fock[6,7] (HF) level. However, due to the fast growing computational cost with system size [$O(N^p)$ where $p \geq 5$ in general], the range of systems that can be modelled by correlated calculations is limited.[8–12]

One way to circumvent this scaling curse is quantum embedding.[13–23] Conventionally, embedding methods reduce the computational cost by singling out a subset of degrees of freedom and treating them using a high-level theory, while leaving the rest of the system, as well as the interaction with the aforementioned subsystem handled by a low-level theory (i.e., bath). This scheme is particularly useful when there is a natural separation between the degrees of freedom that one desires to investigate and those that are relatively "inert". Such separations could be based on either an energetic criterion or a real-space metric. An example of the former is the complete active space (CAS) methods[24–26] that are often used when a single-reference description of the system fails. Examples of the latter are the various flavors of wave function theory (WFT)-in-density functional theory (DFT) embedding[15,16,27,28] and

DFT-in-DFT embedding,[29–31] which have been demonstrated useful on many systems where the interesting chemistry occurs at a spatially confined region. In what follows, this scheme is referred to as "local embedding".

In addition to local embedding, recent developments have also suggested the possibility of "global embedding". Here, the basic idea is divide and conquer: one partitions a large system into smaller fragments (e.g., in terms of localized orbitals), repeatedly applies the aforementioned local embedding to each fragment, and then assembles local contributions to obtain a global estimate of the desired property. As a more general approach, the global embedding can be applied to systems where a separation of degrees of freedom is vague or does not exist at all. We note that in literature this scheme is also referred to as the fragmentation method[32,33] and represents the "bottom-up" approach to reduced-scaling correlated calculations.

In contrast, a "top-down" approach to reduced-scaling correlated calculations is local correlation theory. In these methods, one starts with a set of fully delocalized equations for the whole system and discards terms that are (hopefully) unimportant to the computation of the desired properties. Since the pioneering works of Pulay and Saebo[34–36] in the 1980s, many research groups have contributed to this field, leading to the developments of a vast number of theories as well as numerical techniques, including Local Møller-Plesset perturbation theory to the second order[37,38] (LMP2), local coupled cluster theory[39–41] (LCC) and its orbital-specific virtual[42,43] (OSV) variant, Laplace transform MP2,[44,45] divide-and-conquer-based MP2[46] and CC[47,48] (DC-MP2 and CC), fragment molecular orbital[49–52] (FMO), tensor hypercontraction[53–55] (THC), to name a few. We particularly mention the domain localized pair natural orbital[56–58] (DLPNO) approach, which represents one of the most popular local correlation methods that has been widely benchmarked[59–63] and used.[64–67]

In this work, we focus on a specific class of global embedding/fragmentation methods based on the Schmidt decomposition.[68–71] Schmidt decomposition preserves the entanglement between fragments and baths which makes it suitable for embedding chemical systems. We

mention here seminal works towards that direction within the framework of density matrix embedding theory[72,73] (DMET) and related methods[74–79] from the Chan group (on simple atomic latices,[73] a chemical reaction,[80] and simple solids[81]), the Gagliardi group (on bond dissociation[82,83] and simple solids[84]), and the Scuseria group (on simple solids[85]). One major challenge faced by these works is that the rigid partition of a system into non-overlapping fragments could cause ambiguity and lead to slow convergence with fragment size.[80,86] The latter is also known to the fragmentation community.[87]

Recently, we have developed bootstrap embedding[86,88–90] (BE) aimed at solving both problems. BE is formulated using overlapping fragments that allow more flexible partitioning of a chemical system and give rise to a set of inter-fragment matching conditions (*vide infra*) that significantly boosts the accuracy of the embedding. Numerical tests have confirmed both the applicability of BE to general molecular systems[89,90] and its fast convergence with fragment size.[90] However, these tests were performed on medium-sized molecules and with a relatively inaccurate high-level solver (MP2[91]) due to the preliminary nature of the implementation.[90]

Here, we show that with a production-level implementation, BE provides an efficient "bottom-up" alternative to local correlation methods for large molecular systems. Specifically, we implement BE with the more accurate coupled cluster with singles and doubles[92,93] (CCSD) local solver, and largely reduce the computational cost by streamlining the fragment choices, developing an efficient integral transform algorithm, and optimizing the algorithm for density matching. We demonstrate our method on conjugated molecular systems containing up to $\sim$ 2900 basis functions in a minimal basis, where BE with reasonably sized fragments consistently recovers $\geq 99.5\%$ of the total correlation energy of a full CCSD calculation. Both the time and space requirements of BE compare favorably to DLPNO-CCSD. We believe these developments represent an important step towards the application of BE to solve practical problems.

This article is organized as follows. In section 2, we briefly review the formalism of BE,

and present the techniques developed in this work towards an efficient implementation. Some details regarding the CCSD implementation are also discussed. In section 3, we articulate the computational details. In section 4, we present results of both the accuracy and computational efficiency of BE compared to DLPNO-CCSD. In section 5, we conclude this work by pointing out several future directions.

2 Theory

2.1 Bootstrap Embedding

Consider the following second-quantized Hamiltonian that describes a chemical system,

$$\hat{H} = \sum_{\mu\nu}^{N} h_{\mu\nu} c_\mu^\dagger c_\nu + \frac{1}{2} \sum_{\mu\nu\lambda\sigma}^{N} V_{\mu\nu\lambda\sigma} c_\mu^\dagger c_\lambda^\dagger c_\sigma c_\nu, \tag{1}$$

where $\mathbf{h}$ and $\mathbf{V}$ are the standard one- and two-electron integrals [in the (11|22) notation], and $c_\mu^\dagger$ (c_ν) creates (annihilates) an electron in a local orbital (LO), $|\phi_\mu\rangle$. In what follows, we assume these LOs form an orthonormal basis. Suppose we have obtained the HF solution, $|\Phi_0\rangle$, to $\hat{H}$. We define a fragment A by specifying a subset of N_A LOs, $\{\phi_\mu\}_{\mu\in A}$ (typically, $N_A \ll N$). Then the HF state has the following product structure[73]

$$|\Phi_0\rangle = \left(\sum_{p=1}^{N_A} \lambda_p^A |f_p^A\rangle \otimes |b_p^A\rangle \right) \otimes |\Phi_0^{\mathrm{env},A}\rangle, \tag{2}$$

Equation (2) is called a Schmidt decomposition of $|\Phi_0\rangle$ on fragment A (see Supporting Information for the algorithmic details) and divides the system into three parts: the fragment orbitals $\{f_p^A\}_{p=1}^{N_A}$ which we choose to be the fragment LOs $\{\phi_\mu\}_{\mu\in N_A}$,[74] the bath orbitals $\{b_p^A\}_{p=1}^{N_A}$ that are entangled with the fragment orbitals, and the environment $|\Phi_0^{\mathrm{env},A}\rangle$ that is disentangled with the fragment orbitals. The $2N_A$ fragment + bath orbitals are called the embedding orbitals (EOs) and span an active space with the environment being a spectator,

giving rise to the following embedding Hamiltonian,

$$\hat{H}^A = E^{\mathrm{env},A} + \sum_{pq}^{2N_A} h^A_{pq} a_p^{A\dagger} a_q^A + \frac{1}{2} \sum_{pqrs}^{2N_A} V^A_{pqrs} a_p^{A\dagger} a_r^{A\dagger} a_s^A a_q^A, \tag{3}$$

where

$$\begin{aligned} E^{\mathrm{env},A} &= \mathrm{Tr}\,(\mathbf{h} + \mathbf{F}^{\mathrm{env},A})\mathbf{P}^{\mathrm{env},A}, \\ h^A_{pq} &= \sum_{\mu\nu}^{N} T^A_{\mu p} F^{\mathrm{env},A}_{\mu\nu} T^A_{\nu q}, \\ V^A_{pqrs} &= \sum_{\mu\nu\lambda\sigma}^{N} T^A_{\mu p} T^A_{\nu q} V_{\mu\nu\lambda\sigma} T^A_{\lambda r} T^A_{\sigma s}, \end{aligned} \tag{4}$$

where $\mathbf{T}^A = [\mathbf{T}^{f,A}|\mathbf{T}^{b,A}]$ is the coefficient matrix of $\{|f_p^A\rangle\}$ and $\{|b_p^A\rangle\}$, $\mathbf{P}^{\mathrm{env},A}$ is the one-particle density matrix (1PDM) of the environment, and $\mathbf{F}^{\mathrm{env},A}$ is the Fock matrix of the environment. Note that $\hat{H}^A$ has no higher order interaction terms, which is an advantage of using a mean-field bath.[94] $\hat{H}^A$ constructed by eqs. (3) and (4) is sometimes said to have an "interacting" bath in the literature.[80]

In BE, we partition a system into N_{frag} overlapping fragments (see section 2.2 for details). For each fragment, the constituent LOs (which are the fragment orbitals by our choice) are recognized as either *center* or *edge* depending on whether a LO lies at the bulk or the surface of the fragment. In general, the wave function on the center LOs is more accurately described by the high-level fragment calculation than the edge ones because the latter interact more strongly with the corresponding (low-level) bath. This surface error leads to the aforementioned slow convergence of traditional fragmentation methods using non-overlapping fragments. When fragments overlap, by contrast, the wave function on the edge LOs of one fragment could be better described in other fragments if they are the center LOs there. This observation suggests an approach to improving the embedding: matching the wave function (e.g., in terms of density matrix) on the edge LOs of each fragment to that on the corresponding center LOs of other fragments. This idea is schematically illustrated

in fig. 1.

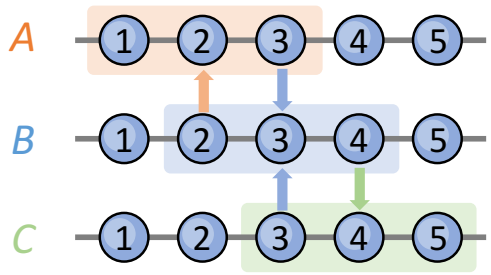

Figure 1: Schematic illustration of BE density matching. LO 2 (or atom 2, see section 2.2) is the center LO (atom) in fragment A and the edge LO (atom) in fragment B. Hence, we match the wave function on LO (atom) 2 in fragment B to that in fragment A (orange up arrow). Other arrows can be understood in a similar way.

Mathematically, the intuition above can be formulated as a set of constrained optimizations. Consider two overlapping fragments, A and B. Let $\mathbb{E}_A$ be the set of edge LOs of A and $\mathbb{C}_B$ the center LOs of B. Then, $\mathbb{E}_A \cap \mathbb{C}_B$ denotes the overlapping region where one needs to match the wave function of A to that of B. In this works, we focus on matching elements of the 1PDM of different fragments. The fragment calculation of A is then constrained as follows

$$\begin{aligned} \min_{\Psi^A} \langle \hat{H}^A \rangle_A, \text{ s.t. } \langle a_p^{A\dagger} a_q^A \rangle_A = P_{pq}^B, \\ \forall p, q \in \mathbb{E}_A \cap \mathbb{C}_B, \forall B \neq A \end{aligned} \tag{5}$$

where $\langle \cdots \rangle_A = \langle \Psi^A | \cdots | \Psi^A \rangle$, and we loop over all fragments $B \neq A$ to enumerate all the matching conditions for A. The same analysis can be repeated for all fragments, leading to a set of N_{frag} coupled constrained optimizations that corresponds to the following Lagrangian

$$\begin{aligned} \mathcal{L} = \sum_A^{N_{\text{frag}}} \Bigg[\langle \hat{H}^A \rangle_A - \mathcal{E}^A (\langle \hat{1} \rangle_A - 1) + \\ \sum_{B \neq A}^{N_{\text{frag}}} \sum_{pq \in \mathbb{E}_A \cap \mathbb{C}_B} \lambda_{pq}^A \left(\langle a_p^{A\dagger} a_q^A \rangle_A - P_{pq}^B \right) \Bigg] + \\ \mu \left[\left(\sum_A^{N_{\text{frag}}} \sum_{p \in \mathbb{C}_A} \langle a_p^{A\dagger} a_p^A \rangle_A \right) - N_e \right] \end{aligned} \tag{6}$$

where $\{\lambda^A_{pq}\}$ are the Lagrangian multipliers for the density matching, and μ is a global chemical potential that fixes the total number of electrons [assuming fragment centers do not overlap; see eq. (10) and the discussion there]. Making eq. (6) stationary with respect to Ψ^A leads to an eigenvalue equation for fragment A

$$\left(\hat{H}^A + \sum_{pq\in\mathbb{E}_A} \lambda^A_{pq} a^{A\dagger}_p a^A_q + \mu \sum_{p\in\mathbb{C}_A} a^{A\dagger}_p a^A_p\right)|\Psi^A\rangle = \mathcal{E}^A|\Psi^A\rangle, \tag{7}$$

where the bare embedding Hamiltonian $\hat{H}^A$ [eq. (3)] is dressed by a local effective potential $\hat{\lambda}^A$ as well as a global chemical potential μ. Note that the matching happens only for the fragment orbitals, which are strictly local to each fragment. Also note that $|\Phi_0\rangle$ is kept fixed in the density matching. Although a DMET-style bath optimization[72,73] is possible and straightforward, we do not explore it in this work.

The BE equations [eq. (7)] for different fragments are highly coupled since the target densities $\{P^B_{pq}\}$ in eq. (7) will change after solving the BE equations for the target fragments. To decouple these equations, we adopt an iterative algorithm (algorithm 1) where in each step eq. (7) is solved with fixed target densities obtained from the last cycle. The algorithm is deemed converged when the root mean square error

$$\epsilon = \left[\frac{1}{N_{\text{cons}}} \sum_{A}^{N_{\text{frag}}} \sum_{B\neq A} \sum_{pq\in\mathbb{E}_A\cap\mathbb{C}_B} (P^A_{pq} - P^B_{pq})^2\right]^{1/2} \tag{8}$$

drops below some threshold τ_{BE} (N_{cons} is the total number of constraints). Our previous works suggest that the simple fixed-point algorithm 1 converges quite well in most cases.[89,90] An efficient algorithm for solving eq. (7) will be presented in section 2.4.

Before moving on, we discuss how BE computes global expectation values. Without loss of generality, consider a one-electron operator $\hat{O} = \sum^N_{\mu\nu} O_{\mu\nu} c^\dagger_\mu c_\nu$. For the simple case where

Algorithm 1 BE iteration

Input: N_e, $\{\hat{H}^A\}$, $\{\mathbf{P}^A\}$, τ_{BE}
Initialization: $\mu \leftarrow 0$, $\boldsymbol{\lambda}^A \leftarrow \mathbf{0}\ \forall A$
while $\epsilon > \tau_{\mathrm{BE}}$ **do**
  for $A = 1 : N_{\mathrm{frag}}$ **do**
    $\boldsymbol{\lambda}_A \leftarrow \hat{H}^A, \{\mathbf{P}^B\}, \mu$ ▷ eq. (7)
  end for
  $\mu, \{\mathbf{P}^A\} \leftarrow \{\hat{H}^A, \boldsymbol{\lambda}^A\}, N_e$
  $\epsilon \leftarrow \{\mathbf{P}^A\}$ ▷ eq. (8)
end while

fragments do not overlap,

$$\langle \hat{O} \rangle = \frac{1}{2} \sum_{\mu\nu}^{N} O_{\mu\nu} \sum_{AB}^{N_{\mathrm{frag}}} \delta_{\mu\in A}\delta_{\nu\in B}\big(\langle c_\mu^\dagger c_\nu \rangle_A + \langle c_\mu^\dagger c_\nu \rangle_B\big). \tag{9}$$

Equation (9) is dubbed the "democratic" strategy in DMET[80] since when the two operators of $c_\mu^\dagger c_\nu$ come from different fragments, the average of both local expectations is used. The generalization of eq. (9) to a general many-body operator is straightforward. For the overlapping fragments used in this work (section 2.2), the center LOs of each fragment do not overlap (i.e., $\mathbb{C}_A \cap \mathbb{C}_B = \varnothing.\ \forall A \neq B$) and fully partition the system. As a result, eq. (9) is also applicable to these overlapping fragments by replacing the two δ-functions with $\delta_{\mu\in\mathbb{C}_A}\delta_{\nu\in\mathbb{C}_B}$. We give here an explicit expression for the total BE energy

$$E_{\mathrm{BE}} = \sum_{A}^{N_{\mathrm{frag}}} \sum_{p\in\mathbb{C}_A} \left[\sum_{q}^{2N_A} \left(h_{pq}^A - \frac{1}{2} G_{pq}^{\mathrm{env},A} \right) P_{pq}^A + \frac{1}{2} \sum_{qrs}^{2N_A} V_{pqrs}^A \Gamma_{pqrs}^A \right], \tag{10}$$

where $\mathbf{G}^{\mathrm{env},A}$ is the Coulomb-exchange part of $\mathbf{F}^{\mathrm{env},A}$; $\{\mathbf{P}^A\}$ and $\{\boldsymbol{\Gamma}^A\}$ are the fragment 1PDMs and 2PDMs (see section 2.5 for more details), respectively. For the more general cases where fragment centers also overlap, one can again take the "democratic" strategy and use the average value computed using all fragment centers for the overlapping region. This strategy was used in our previous work.[90]

2.2 Fragment Choices

In BE, a fragment consists of a set of LOs that are "close" to each other by some measure. Thus, any fragment choices must have a clear definition for the connectivity between LOs. Following this line, we have explored two strategies in our previous works, one based on individual LOs[89] and the other on atoms[90] (i.e., all LOs centered on the same atom are regarded as the minimal unit), and found that the latter leads to faster convergence for mo

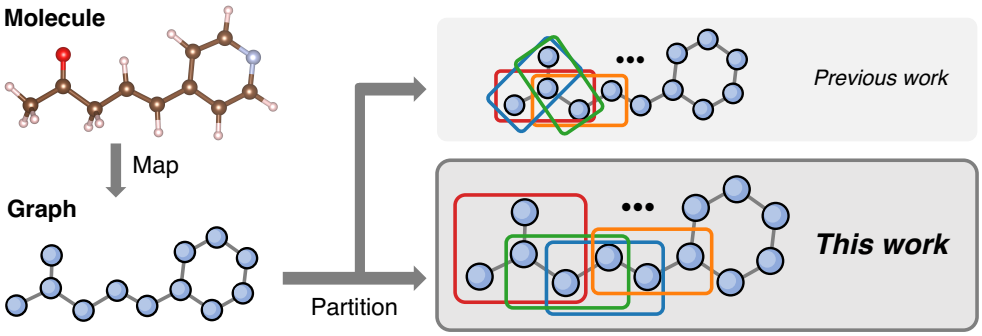

Figure 2: Schematic illustration of partitioning a molecule into overlapping fragments based on atoms and chemical bonds. The old (ref. 90) and new fragment choices are displayed for $m = 3$ and $n = 2$ (see discussion in the main text), respectively. The new scheme generates fewer fragments.

In the original atom-based scheme,[90] a molecule is first mapped onto a graph with its atoms and chemical bonds being the nodes and edges of the graph (fig. 2). Then, all connected subgraphs up to a given size (say, m atoms) are identified as fragments (the case of $m = 3$ is schematically illustrated in fig. 2). While being well-defined and applicable to general chemical systems, this scheme generates fragments whose number (N_{frag}) rises quickly with both the fragment size and the dimension of the system due to the recognization of *all* connected subgraphs as fragments. The dependence of N_{frag} on fragment size discourages the use of large fragments that are necessary for accurate BE calculations, while the dependence on dimension limits the range of applicable systems. In addition, a fast growing N_{frag} also raises the space complexity for storing the transformed integrals (see section 2.3).

The problem of the original atom-based scheme is the inclusion of *all* connected subgraphs

as fragments. To that end, we here adopt a simpler fragment definition: the *atom-centered* fragments. In this scheme, each atom is associated with only one fragment composed of (1) that atom and (2) all atoms from up to the $(n-1)$-th coordination shell. Thus, $n = 1$ is the minimal size where every atom is a fragment. $n = 2$ adds the nearest neighbors to each fragment, and $n = 3$ further includes the second-nearest neighbors (the case of $n = 2$ is schematically illustrated in fig. 2). In all cases, the number of atom-centered fragments satisfy $N_{\text{frag}} \leq N_{\text{atom}}$, where "$<$" could happen since for some atoms (e.g., the end atoms of a chain), the corresponding fragments are completely contained in the adjacent fragments and hence are discarded. We note that for the special case of 1D chain-like molecules such as polyacetylenes, the atom-centered scheme with $n = 1, 2, 3, \cdots$ is equivalent to the original atom-based scheme with $m = 1, 3, 5, \cdots$. However, beyond 1D the new scheme generates far fewer fragments compared to the old one, making it suitable for large-scale molecular calculations. We also note that due to the inclusion of the most important local interactions for each atom, the performance of BE based on the atom-centered fragments is not degraded, as will be clear from the numerical results in section 4.

2.3 Integral Transform

Like many other electron correlation methods, one computational bottleneck of BE is the transformation of the electron-repulsion integrals (ERIs) from the atomic orbital (AO) basis to the working basis, which in our case is the EOs for each fragment [eq. (4)]. The naïve algorithm performing such AO-to-EO transform one fragment at a time has the correct fifth-power formal scaling and can be accelerated by standard techniques in literature.[95–101] For overlapping fragments, however, there is a work redundancy problem in the naïve algorithm that we tackle first below.

Consider a fragment A composed of m atoms $\{a_i\}_{i=1}^{m}$, with their respective EO coefficient matrices [eq. (4)] denoted by $\mathbf{T}^A$ and $\{\mathbf{T}^{a_i}\}$. We first note that the EOs of A have the same

span as the EOs of its constituent atoms, i.e.

$$\mathbf{T}^A = \bar{\mathbf{T}}^A \mathbf{U}^A, \tag{11}$$

where $\bar{\mathbf{T}}^A = [\mathbf{T}^{a_1}|\cdots|\mathbf{T}^{a_n}]$ and $\mathbf{U}^A$ is a full rank square matrix (see Supporting Information for details). Equation (11) suggests that the EOs of a fragment can be reconstructed from the EOs of its constituent atoms. Consequently, the embedding ERIs of a fragment can be reconstructed from the embedding ERIs of its constituent atoms, too. This can be seen by substituting eq. (11) into eq. (4), which gives

$$V^A_{pqrs} = \sum_{tuvw}^{2N_A} \bar{V}^A_{tuvw} U^A_{tp} U^A_{uq} U^A_{vr} U^A_{ws}, \tag{12}$$

where

$$\bar{V}^A_{tuvw} = \sum_{\mu\nu\lambda\sigma}^{N} V_{\mu\nu\lambda\sigma} \bar{T}^A_{\mu p} \bar{T}^A_{\nu q} \bar{T}^A_{\lambda r} \bar{T}^A_{\sigma s} \tag{13}$$

is a four-tensor tiled by the ERIs of all the atom-quartets (a_i, a_j, a_k, a_l) formed from A's constituent atoms,

$$V^{(a_i,a_j,a_k,a_l)}_{tuvw} = \sum_{\mu\nu\lambda\sigma}^{N} V_{\mu\nu\lambda\sigma} T^{a_i}_{\mu t} T^{a_j}_{\nu u} T^{a_k}_{\lambda v} T^{a_l}_{\sigma w}. \tag{14}$$

Note that eq. (14) scales as $O(N^4 N_a)$ for each atom-quartet (N_a is the number of LOs on atom a), which is much more expensive than the *local* transform eq. (12), which scales as $O(N_A^5)$.

Now consider the case where $l \geq 2$ fragments overlap. From the discussion above, it is clear that the embedding ERIs of all l fragments can be reconstructed from the embedding ERIs of all the *unique* atom-quartets formed from the atoms underlying all l fragments. This observation suggests a two-step algorithm for the ERI transform:

1. perform the expensive AO-to-EO ERI transform eq. (14) for all unique atom-quartets from the l fragments;

2. perform the fast local transform eq. (12) for each fragment to recover the fragment ERIs from the atom-quartet ERIs.

Here, the key saving is from the fact that the overlapping fragments share the same set of atom-quartet ERIs in the overlapping region, and hence the expensive AO-to-EO transform eq. (14) needs to be performed only once for these EOs. In contrast, in the naïve algorithm these transforms are repeated l times (one for each fragment), which results in redundant computation. The set of unique atom-quartets in step 1 is called the *connected* atom-quartets for a set of overlapping fragments, and represents the minimum work needed for transforming a four-tensor. Similarly, the connected atom-*pairs* represent the minimum work for transforming two indices.

Having resolved the work redundancy problem, we briefly discuss two standard techniques that further lower the computational cost. First, the fifth-power scaling can be reduced to $O(N^3)$ via integral screening using the Cauchy-Schwarz inequality,[99–102]

$$|V_{\mu\nu\lambda\sigma}| \leq \sqrt{J_{\mu\nu} J_{\lambda\sigma}}, \tag{15}$$

where $J_{\mu\nu} = V_{\mu\nu\mu\nu}$. For large molecules described by local basis functions (AOs in our case), the number of significant shell-pairs (N_{sp}), i.e. those satisfying

$$J_{\mu\nu} \geq \tau_{\text{sp}} \tag{16}$$

for some threshold τ_{sp}, grows only linearly with N, resulting in $O(N^2)$ significant ERIs and hence an $O(N^3)$ scaling for the ERI transform. Second, we use density fitting[95–98] (DF) to resolve the ERIs

$$V_{\mu\nu\lambda\sigma} \approx \sum_{P}^{N_{\text{aux}}} \tilde{V}_{\mu\nu P} \tilde{V}_{P\lambda\sigma}, \tag{17}$$

where P indexes a second, auxiliary basis $\{\chi_P\}_{P=1}^{N_{\text{aux}}}$, and

$$\tilde{V}_{\mu\nu P} = \sum_{Q}^{N_{\text{aux}}} (\mu\nu|Q)[\mathbf{S}^{-1/2}]_{QP}, \tag{18}$$

where $S_{PQ} = (P|Q)$. The number of significant elements in $\tilde{\mathbf{V}}$ still scales quadratically with system size after integral screening, but the pre-factor is largely reduced since typically $N_{\text{aux}} \ll N_{\text{sp}}$.

Algorithm 2 BE ERI transform

Input: $\{\mathbf{T}^a\}_{a=1}^{N_{\text{atom}}}$, $\{\mathbf{U}^A\}_{A=1}^{N_{\text{frag}}}$, $\{(a_i, a_j)\}_{\widetilde{ij}=1}^{N_{\text{ap}}}$, $\{(a_i, a_j, a_k, a_l)\}_{\widetilde{ijkl}=1}^{N_{\text{aq}}}$.
for $\widetilde{ij} = 1 : N_{\text{ap}}$ **do**
  $\tilde{V}_{tuP}^{\widetilde{ij}} \leftarrow \sum_{\mu\nu}^{N} \tilde{V}_{\mu\nu P} T_{\mu t}^{a_i} T_{\nu u}^{a_j}$ ▷ eq. (18)
end for
for $\widetilde{ijkl} = 1 : N_{\text{aq}}$ **do**
  $V_{tuvw}^{\widetilde{ijkl}} \leftarrow \sum_{P}^{N_{\text{aux}}} \tilde{V}_{tuP}^{\widetilde{ij}} \tilde{V}_{Pvw}^{\widetilde{kl}}$ ▷ eq. (17)
end for
for $A = 1 : N_{\text{frag}}$ **do**
  $V_{pqrs}^{A} \leftarrow \sum_{tuvw}^{2N_A} \bar{V}_{tuvw}^{A} U_{pt}^{A} U_{qu}^{A} U_{rv}^{A} U_{sw}^{A}$ ▷ eqs. (12) and (13)
end for

On the basis of all above, we present our efficient ERI transform algorithm in algorithm 2, where we extend the two-step algorithm from above to accommodate integral screening and DF. The aforementioned connected atom-pairs and quartets are respectively denoted by $\{(a_i, a_j)\}_{\widetilde{ij}=1}^{N_{\text{ap}}}$ and $\{(a_i, a_j, a_k, a_l)\}_{\widetilde{ijkl}=1}^{N_{\text{aq}}}$ in algorithm 2. The time and space complexities of each step are tabulated in table 1. For a fixed fragment size, the overall computational scaling is $O(N^3)$ in time for the AO-to-EO transform of all connected atom-pairs (first loop in algorithm 2) and $O(N)$ in space for storing the final results $\{\mathbf{V}^A\}$. Note that the $O(N^2)$ storage requirement of the first step can be readily handled through batching the loop over shell-pairs. Indeed, for the largest calculation in this work (BE3 on C_{720}), the peak memory footprint of the first step is only ~ 20 GB after batching, which is much smaller compared to the fragment ERIs (~ 50 GB). We also note that the $O(N^3)$ time complexity can be further lowered to $O(N^2)$ by using local DF,[38,41,103,104] which we will explore in a subsequent work.

Table 1: Time and space complexities of the three loops in algorithm 2. N_a and N_A are the typical size for an atom and a fragment (in terms of the number of LOs), respectively. N_{ap} and N_{aq} are the number of connected atom-pairs and quartets, respectively.

Loop	Time	Space
$\widetilde{ij}$	$O(N_{\text{ap}}N_{\text{sp}}N_{\text{aux}}N_a^2)$	$O(N_{\text{ap}}N_{\text{aux}}N_a^2)$
$\widetilde{ijkl}$	$O(N_{\text{aq}}N_{\text{aux}}N_a^4)$	$O(N_{\text{aq}}N_a^4)$
A	$O(N_{\text{frag}}N_A^5)$	$O(N_{\text{frag}}N_A^4)$

2.4 Density Matching

In addition to the integral transform, the determination of the BE matching potentials ($\{\hat{\lambda}^A\}$) represents a second computational bottleneck. Mathematically, for each fragment one solves the following non-linear system of equations

$$P^A_{pq}(\boldsymbol{\lambda}^A) = P^B_{pq}, \quad \forall p,q \in \mathbb{E}_A \cup \mathbb{C}_B, \forall B \neq A \tag{19}$$

to determine the matching potential, $\hat{\lambda}^A$, in terms of its matrix elements, $\boldsymbol{\lambda}^A$. This step naturally scales linearly with system size [because $N_{\text{frag}} \sim O(N)$] but our previous implementation based on the Newton's method to solve eq. (19) has a huge pre-factor.[90] In the Newton's method,[105] the Jacobian matrix, $\mathbf{J}^A = \nabla_{\boldsymbol{\lambda}^A}\boldsymbol{P}^A$, is built and inverted in each cycle. The time complexity of a Jacobian build is $O(N^A_{\text{cons}})$ for each fragment (using either finite-difference or analytic gradients) with N^A_{cons} the total number of 1PDM elements being constrained for fragment A. Since N^A_{cons} grows rapidly with fragment size (larger fragments have higher chance to overlap), this again hinders the use of large fragments which are necessary for accurate embedding calculations.

In this work, we instead use a quasi-Newton method, the BFGS algorithm,[105] to solve eq. (19). In BFGS, an approximate Jacobian is refined at every cycle using only the value (as opposed to the gradient) of the density matrix elements. This reduces the per-cycle computational cost to $O(1)$. Compared to the Newton's method, however, BFGS could take more cycles to converge when the initial Jacobian is poor. To that end, we find that

the HF Jacobian, which can be computed analytically by solving the coupled perturbed HF (CPHF) equation,[106] is a cost-effective choice. Numerical tests show that the BFGS algorithm with a HF initial Jacobian typically converges in < 10 cycles for solving eq. (19), and this number is only weakly dependent on the fragment size (fig. S4), leading to an $O(1)$ overall computational cost for each fragment. In addition, although we focus on CCSD in this work, tests using other local solvers also show similar convergence rates, which renders the BFGS + HF initial Jacobian approach promising for general use in BE.

2.5 CCSD Density Matrices

As seen in section 2.1, computing the BE total energy requires 1PDM and 2PDM from each fragment calculation. For CCSD, there are two ways to define these density matrices (DMs). The *unrelaxed* CCSD DMs are defined as[107]

$$\begin{aligned} P^{\text{unrlx}}_{pq} &= \langle \Phi_0 | \mathrm{e}^{-\hat{T}} a^\dagger_p a_q \mathrm{e}^{\hat{T}} | \Phi_0 \rangle, \\ \Gamma^{\text{unrlx}}_{pqrs} &= \langle \Phi_0 | \mathrm{e}^{-\hat{T}} a^\dagger_p a^\dagger_r a_s a_q \mathrm{e}^{\hat{T}} | \Phi_0 \rangle, \end{aligned} \tag{20}$$

where

$$\hat{T} = \sum_{ia} t_{ia} a^\dagger_a a_i + \frac{1}{4} \sum_{ijab} t_{iajb} a^\dagger_a a_i a^\dagger_b a_j, \tag{21}$$

where t_{ia} and t_{iajb} are the standard CCSD excitation amplitudes.[6,107] The *relaxed* CCSD DMs are defined as[108,109]

$$\begin{aligned} P^{\text{rlx}}_{pq} &= \langle \Lambda_0 | \mathrm{e}^{-\hat{T}} a^\dagger_p a_q \mathrm{e}^{\hat{T}} | \Phi_0 \rangle, \\ \Gamma^{\text{rlx}}_{pqrs} &= \langle \Lambda_0 | \mathrm{e}^{-\hat{T}} a^\dagger_p a^\dagger_r a_s a_q \mathrm{e}^{\hat{T}} | \Phi_0 \rangle, \end{aligned} \tag{22}$$

where $\langle \Lambda_0 | = \langle \Phi_0 | (\hat{1} + \hat{\Lambda})$, and

$$\hat{\Lambda} = \sum_{ia} \lambda_{ia} a^\dagger_i a_a + \frac{1}{4} \sum_{ijab} \lambda_{iajb} a^\dagger_i a_a a^\dagger_j a_b, \tag{23}$$

where λ_{ia} and λ_{iajb} are the standard CCSD de-excitation amplitudes[107] (or the Lagrangian multipliers in the variational formulation of CC[110]).

When traced with the Hamiltonian, both DMs give the correct CCSD total energy and hence are suitable for evaluating the BE energy using eq. (10). In terms of computational efficiency, the unrelaxed definition [eq. (20)] is preferred since it does not require solving for the de-excitation amplitudes. The relaxed DMs [eq. (22)], on the other hand, have an extra advantage of giving the correct first-order response properties.[108,109] Indeed, the relaxed CCSD DMs have been used to evaluate the DMET energy by other authors.[80,81,85] However, for all systems tested in this work, numerical calculations suggest that BE based on the unrelaxed DMs gives consistently better estimate for the total energy compared to the relaxed ones (figs. S1 and S2). For this reason, results reported below are all based on the unrelaxed CCSD DMs. While the source of this unanticipated result is still under investigation, we note that similar results have been observed in our previous work using MP2 as the local solver for BE.[90]

3 Computational Details

In what follows, we benchmark the accuracy and computational efficiency of BE on a series of molecular systems of increasing size. The molecular structures are provided in Supporting Information. BE is implemented in `frankenstein`[111] that uses `Libint2`[112] for integral evaluation and `PySCF`[113] for the CCSD solver. The spin-restricted HF (RHF) and spin-restricted CCSD are used as the low- and high-level theories, respectively.

As discussed in ref. 90, Schmidt decomposition-based embedding is not efficient for recovering the dynamic correlation in large basis sets and is best regarded as an approach to full-valence active space (FVAS) calculations. We hence use a minimal basis (STO-3G[114]) for all calculations in this work with def2-SVP/C[115] as the auxiliary basis for DF. A true FVAS implementation will be presented in a future work.

To avoid bath disentanglement[90] and reduce computational cost, core molecular orbitals (MOs) are frozen as in previous works.[85] The remaining MOs (both occupieds and virtuals) are then localized by the Foster-Boys scheme[116] to obtain the orthonormal LO basis. We note that the known difficulties of localizing virtual orbitals[87,117] are not observed here due to the use of a minimal basis. For the FVAS calculations in larger bases, other strategies that avoid explicit orbital localizations[34,118] could potentially be used.

BE calculations using the atom-centered fragments up to $n = 3$ (see section 2.2) are considered in this work and are denoted by BEn. The BE iteration is deemed converged when the density matching error eq. (8) drops below $\tau_{\mathrm{BE}} = 10^{-6}$, which roughly translates to an error of $10^{-5} \sim 10^{-4}\, E_h$ for the correlation energy. Since the computed BE correlation energy is relatively insensitive to the shell-pair screening eq. (16), a relatively large threshold ($\tau_{\mathrm{sp}} = 10^{-4}$) is employed, which introduces an error of $\sim 10^{-5}\, E_h$ that is below the convergence threshold above.

The total correlation energy from a full CCSD calculation (frozen core but no DF) using `PySCF` is used as benchmark whenever possible. We also compare BE to a local correlation method, DLPNO-CCSD, as implemented in `ORCA`[119] whenever possible (frozen core and DF using the same auxiliary basis). The standard parameters (e.g., thresholds for pair-selection) in `ORCA` are used for DLPNO-CCSD and no attempts are made to tune them for the specific systems studied in this work.

Finally, all timing data reported below are the wall time recorded on a single computational node that has 16 Intel E5-2650@2.00GHz CPU cores, 64 GB of memory, and 500 GB of disk space. Any calculations requiring more memory/disk space are deemed failed. The most time-consuming steps in the BE integral transform are formulated as matrix multiplications and multithreaded by `OpenMP`, while the BE iteration is parallelized trivially since different fragment calculations are independent. In both steps, a $10 \sim 12$-fold speedup is observed on the 16-core machine mentioned above. For CCSD and DLPNO-CCSD, the default parallelism provided by the respective software packages is used.

4 Results and Discussion

4.1

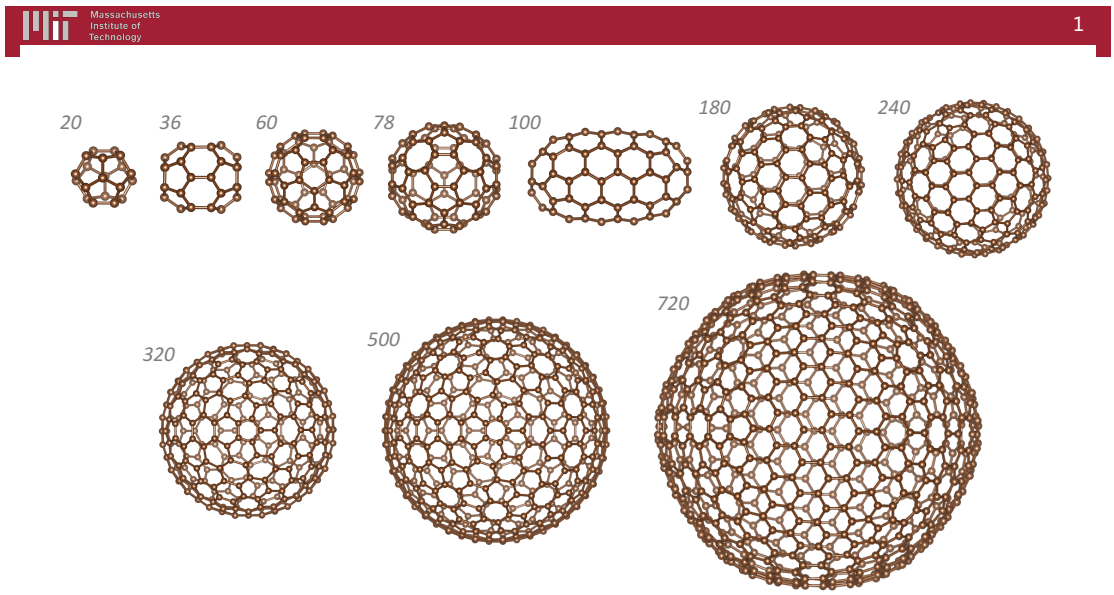

Figure 3: Molecular structure of the fullerene series studied in this work. The number of carbon atoms for each molecule is shown in grey.

We first study a series of fullerene molecules ranging from 20 to 720 carbon atoms (fig. 3). The smaller ones in this series (e.g., C_{20}, C_{36}, and C_{60}) have been extensively studied at various levels of theory,[120–123] while the larger ones have been investigated only by more approximate methods.[124,125] Some of them exhibit strong electron correlation in the ground state, while others do not or are still in debate.[126,127] The versatile electronic structure of these molecules render them a good test bed for benchmarking our method.

To benchmark the effect of fragment size and matching conditions on the accuracy of BE, we first focus on $C_{20} \sim C_{100}$ where the full CCSD results are available. In fig. 4, we present the relative error of the total correlation energy computed by BE2 and BE3. The DLPNO-CCSD results are also included for comparison. For these molecules, the fragments in BE2 and BE3 consist of 4 and 10 atoms, respectively. For BE2, adjacent fragments overlap through individual atoms, and the intra-atomic populations and coherences are matched between fragments. For BE3, fragments overlap through individual atoms and/or two adjacent atoms (i.e., chemical bonds). Hence, one can choose to match only the intra-atomic properties on

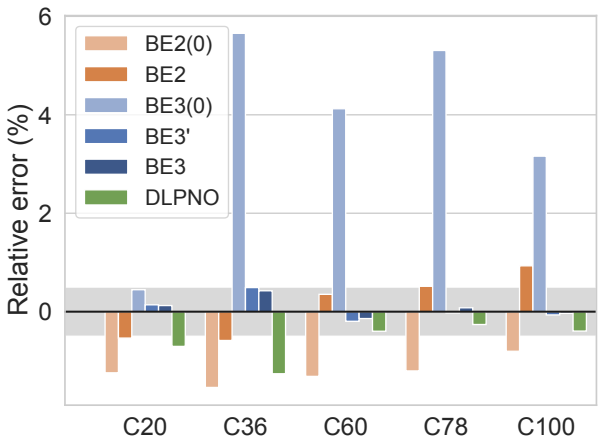

Figure 4: Percentage error of the total correlation energy computed by BE (with different-sized fragments and matching conditions, see the main text) and DLPNO-CCSD for five E-polyacetylene fullerene molecules. BEn(0) denotes the one-shot calculation without density matching. One can see that the error of BE3/BE3' is consistently below $\pm 0.5\%$ (highlited in grey).

individual atoms (denoted by BE3' in fig. 4) or additionally the inter-atomic coherences across chemical bonds (denoted by BE3 in fig. 4). For both BE2 and BE3, we also present the one-shot results (i.e., without density matching) for comparison [denoted by BEn(0)].

Several observations can be made from fig. 4. First and perhaps quite remarkably, without density matching the error of BE3(0) is consistently higher than that of BE2(0) in almost all cases [except for C_{20} where BE3(0) with 10-atom fragments almost amounts to a full CCSD calculation]. This should be compared to the calculations with density matching which, in sharp contrast, greatly reduce the error of the one-shot results [BE2 vs BE2(0); BE3/BE3' vs BE3(0)] and show monotonic convergence with fragment size (BE3/BE3' vs BE2). These observations highlight the importance of reducing the surface error of the embedded fragments, which in BE is achieved self-consistently through the inter-fragment density matching. Second, the improvement obtained by matching the coherences across chemical bonds in BE3 is marginal for these molecules: both BE3 and BE3' deliver very accurate results that falls in the window of $\pm 0.5\%$ of error in all cases. This performance is comparable to that of DLPNO-CCSD, even though they approximate the full-system

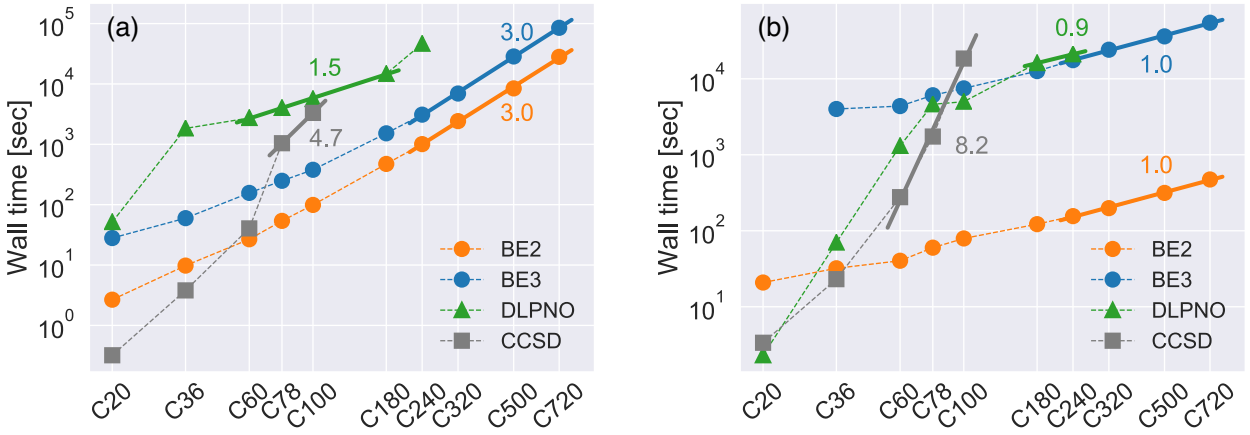

Figure 5: Computational time of (a) the integral transform and (b) the first CCSD cycle (for BE, the first BE iteration cycle) for BE2, BE3, DLPNO-CCSD and CCSD applied to a series of fullerene molecules. The apparent scaling factor γ obtained from fitting to $aN^\gamma + b$ is reported for each series of data. BE exhibits the expected cubic (for integral transform) and linear (for BE iteration) scaling and compares favorably to DLPNO.

Having established the accuracy of BE, we now turn to benchmark its computational efficiency using all molecules shown in fig. 3. The wall time of the BE integral transform and the first BE iteration cycle is presented in fig. 5 together with both CCSD and DLPNO-CCSD for comparison (for these two, the time of the first CCSD cycle is plotted in fig. 5b). The apparent scaling factor γ is labelled for each series of data. For CCSD and DLPNO-CCSD, we managed to obtain results up to C_{100} and C_{240}, respectively. Larger calculations failed due to exceeding the memory and/or disk space limit (section 3).

For the integral transform (fig. 5a), BE displays the expected $O(N^3)$ scaling owing to the integral screening [eqs. (15) and (16)]. The cubic scaling of BE is lower than the fifth-power scaling of full CCSD but still higher than the almost linear scaling [$O(N^{1.5})$] of DLPNO due to the use of global DF as discussed in section 2.3. Nevertheless, the wall time of BE3 is an order of magnitude lower than that of DLPNO for almost all cases, and also becomes lower than the full CCSD starting from C_{78}. This observation indicates that for these quasi-2D, conjugated systems, the embedding strategy ("bottom-up") can be more efficient in exploring the locality of the electron correlation than the local correlation scheme ("top-

down"), potentially due to the small HOMO-LUMO gaps degrading the effectiveness of the latter (e.g., the pair selection process in DLPNO). This efficiency difference is also reflected in the storage requirement: the integral transform of BE can be performed completely in memory (except for the final results, which are stored on disk) even for the largest calculation (C_{720}/BE3). DLPNO, by contrast, requires more than 500 GB of disk space for C_{320} using the standard parameters in `ORCA`.

For the iteration step (fig. 5b), BE displays the expected linear scaling similar to DLPNO [$O(N^{0.9})$]. BE3 also becomes comparable to DLPNO in the actual computational time starting at C_{78}. The computational efficiency of BE, as discussed above, is a result of both an improved density matching algorithm (section 2.4) and a streamlined fragment choice (section 2.2). We also emphasize the importance of different fragment calculations being independent, which leads to constantly high parallelism of BE especially for large systems (section 3). In contrast, the parallelism of `PySCF`'s full CCSD calculations degrades as system size grows, leading to an eighth-power apparent scaling that is much higher than the $O(N^6)$ formal scaling.

It is also interesting to note how differently the computational cost grows with fragment size in the two steps: BE3 is ~ 3 times slower than BE2 for the integral transform (fig. 5a), but the ratio raises to > 100 for the iteration step (fig. 5b). Such a large difference can be understood from the scaling dependence on the fragment size for each step. The integral transform scales linearly with fragment size through the dependence on N_{ap} (table 1), while the BE iteration scales as the sixth-power with fragment size when using CCSD as the local solver. However, since the integral transform dominates the overall cost for large molecules, the overall cost of BE grows only linearly with fragment size in this size regime. This mild dependence on fragment size is crucial for obtaining the accurate BE3 results in fig. 4.

4.2 *E*-polyacetylenes

In the above example, BE displays comparable or even higher computational efficiency compared to the more established local correlation method, DLPNO. This trend, however, does

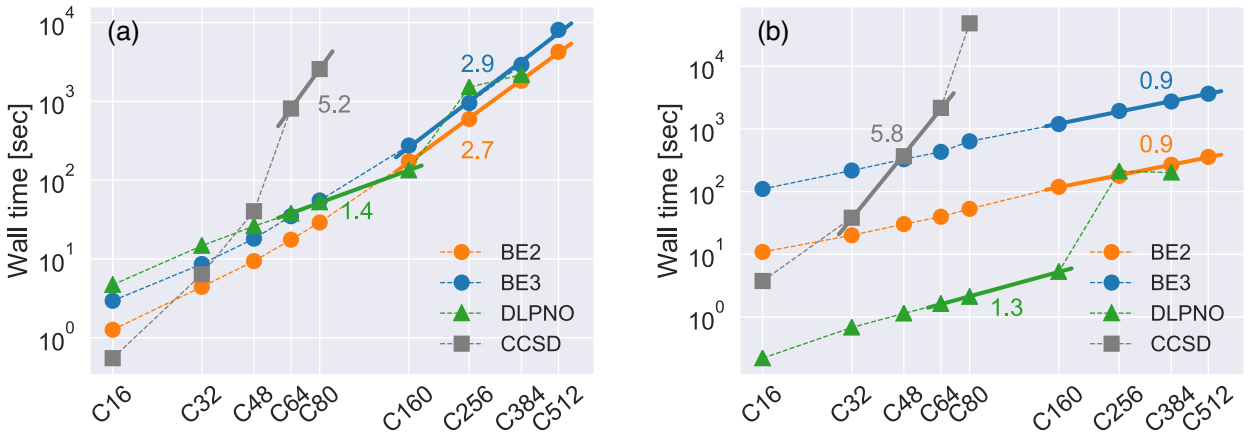

Figure 6: Computational time of (a) the integral transform and (b) the first CCSD cycle (for BE, the first BE iteration cycle) for BE2, BE3, DLPNO-CCSD and CCSD applied to a series of *E*-polyacetylene molecules (C_{2k} in the x-axis is short for $C_{2k}H_{2k+2}$). The apparent scaling factor γ obtained from fitting to $aN^\gamma + b$ is reported for each series of data. Note that the DLPNO wall time of both steps increases abruptly at C_{160}, which is attributed to the increased size of the ERIs eventually exceeding the memory limit of 4 GB per CPU core (section 3) beyond C_{160} (fig. S5 and table S2).

The timing data that parallel fig. 5 are presented in fig. 6 for *E*-polyacetylenes from 16 to 512 carbon atoms. While BE displays the same apparent scalings as above and becomes faster than full CCSD even for $C_{48}H_{50}$, the relative overhead between BE and DLPNO is much higher compared to the previous example. For the integral transform (fig. 6a), BE3 has a similar wall time compared to DLPNO for small molecules, but becomes slower than DLPNO for larger ones due to the higher computational scaling (cubic vs nearly linear). This comparison highlights the effect of local DF in reducing the computational cost especially for systems of low dimensions. Another con of using global DF is the need to invert an $N_{\text{aux}} \times N_{\text{aux}}$ matrix $[\mathbf{S}]_{PQ}$ in eq. (18), which poses a numerical challenge for large molecules.

Indeed, even though the extrapolated wall time from fig. 6a suggests that a BE3 calculation could be performed for $C_{1024}H_{1026}$ in $\sim 10^5$ s, in practice the Cholesky decomposition fails for inverting $[\mathbf{S}]_{PQ}$ even for E-polyacetylenes beyond $C_{512}H_{514}$.

For the iteration step (fig. 6b), the wall time of both BE2 and BE3 is significantly higher than that of DLPNO in almost all cases. A detailed examination of the BE calculations suggests that the BFGS algorithm (section 2.4) still performs very well for solving eq. (19) (convergence achieved in $3 \sim 5$ cycles for all fragments and all molecules). Thus, the large overhead of the BE iteration observed here mainly reflects the inefficiency of the local solver itself: the regular CCSD solver could be adapted to better exploit the locality structure of the embedding Hamiltonians.

Despite the loss in computational efficiency, the accuracy of BE follows a similar trend as in the previous example. A figure that parallels fig. 4 for the first five E-polyacetylene molecules in the series ($16 \sim 80$ carbon atoms) is presented in Supporting Information (fig. S3). As can be seen from the plot, the error of the total correlation energy computed using BE3 and BE3' consistently falls in the window of $\pm 0.2\%$, which is comparable to DLPNO.

5 Conclusion

In conclusion, we show in this work that BE provides an efficient approach to the correlated calculations of large molecules. Specifically, BE with CCSD as the local solver and using atom-centered fragments including up to the second nearest neighbors (i.e., BE3) successfully reproduces the total correlation energy of full CCSD calculations with a typical error less than 0.5%. Both the accuracy and computational efficiency are comparable to the more established local correlation method, DLPNO, making BE a promising candidate for more practical applications.

The implementation of BE presented here can be further improved from several perspectives. First, both the time and space complexities of the BE integral transform can be

reduced by an order of magnitude by replacing the global DF with a local one.[38,41,103,104] Second, the locality of the embedding Hamiltonians could be exploited by the local solver to further lower the overhead of the BE iteration step. These two improvements will render BE more competitive compared to the existing methods.

In the future, BE could be extended in several directions. First, although the relative error of BE energy is low, this accuracy may not translate to the energy change of a reaction due to an "unbalanced" description of different states by BE. Thus, it is necessary to systematically benchmark BE's performance of predicting energy differences in a practical setting. Second, although the Foster-Boys orbitals work well in this work, there are many other options for orbital localization[34,118,128–130] that could potentially further boost the performance of BE. Thus, a systematic investigation on the effect of different LOs is a straightforward but nonetheless very important next step. Third, as long as the integral transform dominates the computational cost, using a local solver beyond CCSD would not significantly increase the computational time but could potentially improve BE's accuracy. Fourth, the minimal-basis implementation developed here could be extended to perform FVAS calculations to recover the valence electron correlation in larger basis sets (e.g., applying BE to the subspace spanned by localized valence orbitals[118]). The remaining electron correlation, mainly weak and dynamic in nature, could potentially be described at a low cost by perturbation theory.[131] In addition, although the fixed RHF bath works well in this work, there are cases where the quality of the bath is important.[72,81] Thus, one can either adopt a better bath wave function[83,94] or perform explicit bath optimization.[81] Last but not least, the theory presented here for molecules is applicable to general chemical systems including solid-state materials. BE hence may offer a convenient approach to the correlated calculations in solids.

Supporting Information (i) Derivation of the Schmidt decomposition of a mean-field state. (ii) Proof of eq. (11). (iii) Comparing the accuracy of BE correlation energy computed using the relaxed and the unrelaxed CCSD DMs. (iv) Error of BE correlation energy of *E*-polyacetylene molecules from $C_{16}H_{18}$ to $C_{80}H_{82}$. (v) Rate of convergence of the BFGS algorithm for different fragment size and matching conditions. (vi) Timing data of selected steps of *E*-polyacetylenes DLPNO calculations. (vii) Structures of all molecules studied in this work.

Acknowledgement

This work was funded by a grant from the NSF (Grant No. CHE-1900358).

References

(1) Theriot, J. C.; Lim, C.-H.; Yang, H.; Ryan, M. D.; Musgrave, C. B.; Miyake, G. M. Organocatalyzed atom transfer radical polymerization driven by visible light. *Science* **2016**, *352*, 1082–1086.

(2) Tawfik, S. A.; Ali, S.; Fronzi, M.; Kianinia, M.; Tran, T. T.; Stampfl, C.; Aharonovich, I.; Toth, M.; Ford, M. J. First-principles investigation of quantum emission from hBN defects. *Nanoscale* **2017**, *9*, 13575–13582.

(3) Huang, W.; Einzinger, M.; Zhu, T.; Chae, H. S.; Jeon, S.; Ihn, S.-G.; Sim, M.; Kim, S.; Su, M.; Teverovskiy, G.; Wu, T.; Van Voorhis, T.; Swager, T. M.; Baldo, M. A.; Buchwald, S. L. Molecular Design of Deep Blue Thermally Activated Delayed Fluorescence Materials Employing a Homoconjugative Triptycene Scaffold and Dihedral Angle Tuning. *Chem. Mater.* **2018**, *30*, 1462–1466.

(4) MacLeod, M. J.; Goodman, A. J.; Ye, H.-Z.; Nguyen, H. V.-T.; Van Voorhis, T.;

Johnson, J. A. Robust gold nanorods stabilized by bidentate N-heterocyclic-carbene-thiolate ligands. *Nat. Chem.* **2019**, *11*, 57 – 63.

(5) Bramley, G.; Nguyen, M.-T.; Glezakou, V.-A.; Rousseau, R.; Skylaris, C.-K. Reconciling Work Functions and Adsorption Enthalpies for Implicit Solvent Models: A Pt (111)/Water Interface Case Study. *J. Chem. Theory Comput.* **2020**, *16*, 2703–2715.

(6) Szabo, A.; Ostlund, N. S. *Modern Quantum Chemistry: Introduction to Advanced Electronic Structure Theory*; Dover Publications Inc.: Mineola, New York, 1996.

(7) Roothaan, C. C. J. New Developments in Molecular Orbital Theory. *Rev. Mod. Phys.* **1951**, *23*, 69–89.

(8) Mabrouk, N.; Berriche, H. Theoretical study of the NaLi molecule: potential energy curves, spectroscopic constants, dipole moments and radiative lifetimes. *J. Phys. B: At. Mol. Opt. Phys* **2008**, *41*, 155101.

(9) Meniailava, D. N.; Shundalau, M. B. Multi-reference perturbation theory study on the CsYb molecule including the spin-orbit coupling. *Comput. Theor. Chem.* **2017**, *1111*, 20 – 26.

(10) Eckhardt, A. K.; Schreiner, P. R. Spectroscopic Evidence for Aminomethylene (H-C̈-NH2)-The Simplest Amino Carbene. *Angew. Chem. Int. Ed.* **2018**, *57*, 5248–5252.

(11) Wilkins, D. M.; Grisafi, A.; Yang, Y.; Lao, K. U.; DiStasio, R. A.; Ceriotti, M. Accurate molecular polarizabilities with coupled cluster theory and machine learning. *Proc. Natl. Acad. Sci.* **2019**, *116*, 3401–3406.

(12) Heim, Z. N.; Amberger, B. K.; Esselman, B. J.; Stanton, J. F.; Woods, R. C.; McMahon, R. J. Molecular structure determination: Equilibrium structure of pyrimidine (m-C4H4N2) from rotational spectroscopy (reSE) and high-level ab initio calculation

(re) agree within the uncertainty of experimental measurement. *J. Chem. Phys.* **2020**, *152*, 104303.

(13) Kotliar, G.; Savrasov, S. Y.; Haule, K.; Oudovenko, V. S.; Parcollet, O.; Marianetti, C. A. Electronic structure calculations with dynamical mean-field theory. *Rev. Mod. Phys.* **2006**, *78*, 865–951.

(14) Huang, C.; Carter, E. A. Potential-functional embedding theory for molecules and materials. *J. Chem. Phys.* **2011**, *135*, 194104.

(15) Manby, F. R.; Stella, M.; Goodpaster, J. D.; Miller, T. F. A Simple, Exact Density-Functional-Theory Embedding Scheme. *J. Chem. Theory Comput.* **2012**, *8*, 2564–2568.

(16) Goodpaster, J. D.; Barnes, T. A.; Manby, F. R.; Miller, T. F. Accurate and systematically improvable density functional theory embedding for correlated wavefunctions. *J. Chem. Phys.* **2014**, *140*, 18A507.

(17) Lan, T. N.; Kananenka, A. A.; Zgid, D. Communication: Towards *ab initio* self-energy embedding theory in quantum chemistry. *J. Chem. Phys.* **2015**, *143*, 241102.

(18) Ye, H.-Z.; Welborn, M.; Ricke, N. D.; Van Voorhis, T. Incremental embedding: A density matrix embedding scheme for molecules. *J. Chem. Phys.* **2018**, *149*, 194108.

(19) Lan, T. N.; Zgid, D. Generalized Self-Energy Embedding Theory. *J. Phys. Chem. Lett.* **2017**, *8*, 2200–2205.

(20) Yu, K.; Carter, E. A. Extending density functional embedding theory for covalently bonded systems. *Proc. Natl. Acad. Sci.* **2017**, *114*, E10861–E10870.

(21) Huang, C. Embedded Cluster Density Approximation for Exchange-Correlation Energy: A Natural Extension of the Local Density Approximation. *J. Chem. Theory Comput.* **2018**, *14*, 6211–6225.

(22) Zhang, X.; Carter, E. A. Subspace Density Matrix Functional Embedding Theory: Theory, Implementation, and Applications to Molecular Systems. *J. Chem. Theory Comput.* **2019**, *15*, 949–960.

(23) Zhu, T.; Cui, Z.-H.; Chan, G. K.-L. Efficient Formulation of *Ab Initio* Quantum Embedding in Periodic Systems: Dynamical Mean-Field Theory. *J. Chem. Theory Comput.* **2020**, *16*, 141–153.

(24) Roos, B. O.; Taylor, P. R.; Sigbahn, P. E. A complete active space SCF method (CASSCF) using a density matrix formulated super-CI approach. *Chem. Phys.* **1980**, *48*, 157 – 173.

(25) Siegbahn, P.; Heiberg, A.; Roos, B.; Levy, B. A Comparison of the Super-CI and the Newton-Raphson Scheme in the Complete Active Space SCF Method. *Phys. Scr.* **1980**, *21*, 323–327.

(26) Siegbahn, P. E. M.; Almlöf, J.; Heiberg, A.; Roos, B. O. The complete active space SCF (CASSCF) method in a Newton-Raphson formulation with application to the HNO molecule. *J. Chem. Phys.* **1981**, *74*, 2384–2396.

(27) Chulhai, D. V.; Goodpaster, J. D. Projection-Based Correlated Wave Function in Density Functional Theory Embedding for Periodic Systems. *J. Chem. Theory Comput.* **2018**, *14*, 1928–1942.

(28) Wen, X.; Graham, D. S.; Chulhai, D. V.; Goodpaster, J. D. Absolutely Localized Projection-Based Embedding for Excited States. *J. Chem. Theory Comput.* **2020**, *16*, 385–398.

(29) Severo Pereira Gomes, A.; Jacob, C. R. Quantum-chemical embedding methods for treating local electronic excitations in complex chemical systems. *Annu. Rep. Prog. Chem., Sect. C: Phys. Chem.* **2012**, *108*, 222–277.

(30) Jacob, C. R.; Neugebauer, J. Subsystem density-functional theory. *Wiley Interdiscip. Rev. Comput. Mol. Sci* **2014**, *4*, 325–362.

(31) Wesolowski, T. A.; Shedge, S.; Zhou, X. Frozen-Density Embedding Strategy for Multilevel Simulations of Electronic Structure. *Chem. Rev.* **2015**, *115*, 5891–5928.

(32) Gordon, M. S.; Fedorov, D. G.; Pruitt, S. R.; Slipchenko, L. V. Fragmentation Methods: A Route to Accurate Calculations on Large Systems. *Chem. Rev.* **2012**, *112*, 632–672.

(33) Gordon, M. S., Ed. *Fragmentation: Towards Accurate Calculations on Complex Molecular Systems*; John Wiley & Sons Ltd, 2017.

(34) Pulay, P. Localizability of dynamic electron correlation. *Chem. Phys. Lett.* **1983**, *100*, 151 – 154.

(35) Pulay, P.; Saebø, S. Orbital-invariant formulation and second-order gradient evaluation in Møller-Plesset perturbation theory. *Theor. Chim. Acta* **1986**, *69*, 357–368.

(36) Saebø, S.; Pulay, P. Fourth-order Møller-Plessett perturbation theory in the local correlation treatment. I. Method. *J. Chem. Phys.* **1987**, *86*, 914–922.

(37) Schütz, M.; Hetzer, G.; Werner, H.-J. Low-order scaling local electron correlation methods. I. Linear scaling local MP2. *J. Chem. Phys.* **1999**, *111*, 5691–5705.

(38) Werner, H.-J.; Manby, F. R.; Knowles, P. J. Fast linear scaling second-order Møller-Plesset perturbation theory (MP2) using local and density fitting approximations. *J. Chem. Phys.* **2003**, *118*, 8149–8160.

(39) Hampel, C.; Werner, H. Local treatment of electron correlation in coupled cluster theory. *J. Chem. Phys.* **1996**, *104*, 6286–6297.

(40) Kats, D.; Korona, T.; Schütz, M. Local CC2 electronic excitation energies for large molecules with density fitting. *J. Chem. Phys.* **2006**, *125*, 104106.

(41) Werner, H.-J.; Schütz, M. An efficient local coupled cluster method for accurate thermochemistry of large systems. *J. Chem. Phys.* **2011**, *135*, 144116.

(42) Yang, J.; Kurashige, Y.; Manby, F. R.; Chan, G. K. L. Tensor factorizations of local second-order Møller-Plesset theory. *J. Chem. Phys.* **2011**, *134*, 044123.

(43) Yang, J.; Chan, G. K.-L.; Manby, F. R.; Schütz, M.; Werner, H.-J. The orbital-specific-virtual local coupled cluster singles and doubles method. *J. Chem. Phys.* **2012**, *136*, 144105.

(44) Häser, M. Møller-Plesset (MP2) perturbation theory for large molecules. *Theor. Chim. Acta* **1993**, *87*, 147–173.

(45) Schäfer, T.; Ramberger, B.; Kresse, G. Quartic scaling MP2 for solids: A highly parallelized algorithm in the plane wave basis. *J. Chem. Phys.* **2017**, *146*, 104101.

(46) Kobayashi, M.; Akama, T.; Nakai, H. Second-order Møller-Plesset perturbation energy obtained from divide-and-conquer Hartree-Fock density matrix. *J. Chem. Phys.* **2006**, *125*, 204106.

(47) Kobayashi, M.; Nakai, H. Extension of linear-scaling divide-and-conquer-based correlation method to coupled cluster theory with singles and doubles excitations. *J. Chem. Phys.* **2008**, *129*, 044103.

(48) Kobayashi, M.; Nakai, H. Divide-and-conquer-based linear-scaling approach for traditional and renormalized coupled cluster methods with single, double, and noniterative triple excitations. *J. Chem. Phys.* **2009**, *131*, 114108.

(49) Kitaura, K.; Ikeo, E.; Asada, T.; Nakano, T.; Uebayasi, M. Fragment molecular orbital method: an approximate computational method for large molecules. *Chem. Phys. Lett.* **1999**, *313*, 701 – 706.

(50) Fedorov, D. G.; Kitaura, K. The importance of three-body terms in the fragment molecular orbital method. *J. Chem. Phys.* **2004**, *120*, 6832–6840.

(51) Khaliullin, R. Z.; Head-Gordon, M.; Bell, A. T. An efficient self-consistent field method for large systems of weakly interacting components. *J. Chem. Phys.* **2006**, *124*, 204105.

(52) Fedorov, D. G.; Kitaura, K. Extending the Power of Quantum Chemistry to Large Systems with the Fragment Molecular Orbital Method. *J. Phys. Chem. A* **2007**, *111*, 6904–6914.

(53) Hohenstein, E. G.; Kokkila, S. I. L.; Parrish, R. M.; Martínez, T. J. Quartic scaling second-order approximate coupled cluster singles and doubles via tensor hypercontraction: THC-CC2. *J. Chem. Phys.* **2013**, *138*, 124111.

(54) Hohenstein, E. G.; Kokkila, S. I. L.; Parrish, R. M.; Martínez, T. J. Tensor Hypercontraction Equation-of-Motion Second-Order Approximate Coupled Cluster: Electronic Excitation Energies in O(N4) Time. **2013**, *117*, 12972–12978.

(55) Parrish, R. M.; Hohenstein, E. G.; Schunck, N. F.; Sherrill, C. D.; Martínez, T. J. Exact Tensor Hypercontraction: A Universal Technique for the Resolution of Matrix Elements of Local Finite-Range N-Body Potentials in Many-Body Quantum Problems. *Phys. Rev. Lett.* **2013**, *111*, 132505.

(56) Riplinger, C.; Pinski, P.; Becker, U.; Valeev, E. F.; Neese, F. Sparse maps–A systematic infrastructure for reduced-scaling electronic structure methods. II. Linear scaling domain based pair natural orbital coupled cluster theory. *J. Chem. Phys.* **2016**, *144*, 024109.

(57) Saitow, M.; Becker, U.; Riplinger, C.; Valeev, E. F.; Neese, F. A new near-linear scaling, efficient and accurate, open-shell domain-based local pair natural orbital coupled cluster singles and doubles theory. *J. Chem. Phys.* **2017**, *146*, 164105.

(58) Guo, Y.; Riplinger, C.; Becker, U.; Liakos, D. G.; Minenkov, Y.; Cavallo, L.; Neese, F. Communication: An improved linear scaling perturbative triples correction for the domain based local pair-natural orbital based singles and doubles coupled cluster method [DLPNO-CCSD(T)]. *J. Chem. Phys.* **2018**, *148*, 011101.

(59) Minenkov, Y.; Chermak, E.; Cavallo, L. Accuracy of DLPNO-CCSD(T) Method for Noncovalent Bond Dissociation Enthalpies from Coinage Metal Cation Complexes. *J. Chem. Theory Comput.* **2015**, *11*, 4664–4676.

(60) Paulechka, E.; Kazakov, A. Efficient DLPNO-CCSD(T)-Based Estimation of Formation Enthalpies for C-, H-, O-, and N-Containing Closed-Shell Compounds Validated Against Critically Evaluated Experimental Data. **2017**, *121*, 4379–4387.

(61) Shang, Y.; Ning, H.; Shi, J.; Wang, H.; Luo, S.-N. Benchmarking dual-level MS-Tor and DLPNO-CCSD(T) methods for H-abstraction from methyl pentanoate by an OH radical. **2019**, *21*, 20857–20867.

(62) Liakos, D. G.; Guo, Y.; Neese, F. Comprehensive Benchmark Results for the Domain Based Local Pair Natural Orbital Coupled Cluster Method (DLPNO-CCSD(T)) for Closed- and Open-Shell Systems. **2020**, *124*, 90–100.

(63) Schmitz, G.; Elm, J. Assessment of the DLPNO Binding Energies of Strongly Noncovalent Bonded Atmospheric Molecular Clusters. *ACS Omega* **2020**, *5*, 7601–7612.

(64) Mielczarek, D. C.; Nait Saidi, C.; Paricaud, P.; Catoire, L. Generalized Prediction of Enthalpies of Formation Using DLPNO-CCSD(T) Ab Initio Calculations for Molecules Containing the Elements H, C, N, O, F, S, Cl, Br. *J. Comput. Chem.* **2019**, *40*, 768–793.

(65) Maity, B.; Minenkov, Y.; Cavallo, L. Evaluation of experimental alkali metal ion-ligand noncovalent bond strengths with DLPNO-CCSD(T) method. *J. Chem. Phys.* **2019**, *151*, 014301.

(66) Svatunek, D.; Pemberton, R. P.; Mackey, J. L.; Liu, P.; Houk, K. N. Concerted [4 + 2] and Stepwise (2 + 2) Cycloadditions of Tetrafluoroethylene with Butadiene: DFT and DLPNO-UCCSD(T) Explorations. *J. Org. Chem.* **2020**, *85*, 3858–3864.

(67) Manna, D.; Lo, R.; Hobza, P. Spin modification of iron(ii) complexes via covalent (dative) and dispersion guided non-covalent bonding with N-heterocyclic carbenes: DFT, DLPNO-CCSD(T) and MCSCF studies. *Dalton Trans.* **2020**, *49*, 164–170.

(68) Ekert, A.; Knight, P. L. Entangled quantum systems and the Schmidt decomposition. *Am. J. Phys.* **1995**, *63*, 415–423.

(69) Klich, I. Lower entropy bounds and particle number fluctuations in a Fermi sea. *J. Phys. A: Math. Gen.* **2006**, *39*, L85.

(70) Peschel, I.; Eisler, V. Reduced density matrices and entanglement entropy in free lattice models. *J. Phys. A: Math. Theor.* **2009**, *42*, 504003.

(71) Peschel, I. Special Review: Entanglement in Solvable Many-Particle Models. *Braz. J. Phys.* **2012**, *42*, 267–291.

(72) Knizia, G.; Chan, G. K.-L. Density Matrix Embedding: A Simple Alternative to Dynamical Mean-Field Theory. *Phys. Rev. Lett.* **2012**, *109*, 186404.

(73) Knizia, G.; Chan, G. K.-L. Density Matrix Embedding: A Strong-Coupling Quantum Embedding Theory. *J. Chem. Theory Comput.* **2013**, *9*, 1428–1432.

(74) Bulik, I. W.; Scuseria, G. E.; Dukelsky, J. Density matrix embedding from broken symmetry lattice mean fields. *Phys. Rev. B* **2014**, *89*, 035140.

(75) Senjean, B.; Nakatani, N.; Tsuchiizu, M.; Fromager, E. Site-occupation embedding theory using Bethe ansatz local density approximations. *Phys. Rev. B* **2018**, *97*, 235105.

(76) Senjean, B. Projected site-occupation embedding theory. *Phys. Rev. B* **2019**, *100*, 035136.

(77) Fertitta, E.; Booth, G. H. Energy-weighted density matrix embedding of open correlated chemical fragments. *J. Chem. Phys.* **2019**, *151*, 014115.

(78) Lin, L.; Lindsey, M. Variational embedding for quantum many-body problems. 2019.

(79) Tran, H. K.; Van Voorhis, T.; Thom, A. J. W. Using SCF metadynamics to extend density matrix embedding theory to excited states. *J. Chem. Phys.* **2019**, *151*, 034112.

(80) Wouters, S.; Jiménez-Hoyos, C. A.; Sun, Q.; Chan, G. K.-L. A Practical Guide to Density Matrix Embedding Theory in Quantum Chemistry. *J. Chem. Theory Comput.* **2016**, *12*, 2706–2719, PMID: 27159268.

(81) Cui, Z.-H.; Zhu, T.; Chan, G. K.-L. Efficient Implementation of *Ab Initio* Quantum Embedding in Periodic Systems: Density Matrix Embedding Theory. *J. Chem. Theory Comput.* **2020**, *16*, 119–129.

(82) Pham, H. Q.; Bernales, V.; Gagliardi, L. Can Density Matrix Embedding Theory with the Complete Activate Space Self-Consistent Field Solver Describe Single and Double Bond Breaking in Molecular Systems? *J. Chem. Theory Comput.* **2018**, *14*, 1960–1968.

(83) Hermes, M. R.; Gagliardi, L. Multiconfigurational Self-Consistent Field Theory with Density Matrix Embedding: The Localized Active Space Self-Consistent Field Method. *J. Chem. Theory Comput.* **2019**, *15*, 972–986.

(84) Pham, H. Q.; Hermes, M. R.; Gagliardi, L. Periodic Electronic Structure Calculations with the Density Matrix Embedding Theory. *J. Chem. Theory Comput.* **2020**, *16*, 130–140.

(85) Bulik, I. W.; Chen, W.; Scuseria, G. E. Electron correlation in solids via density embedding theory. *J. Chem. Phys.* **2014**, *141*, 054113.

(86) Welborn, M.; Tsuchimochi, T.; Van Voorhis, T. Bootstrap embedding: An internally consistent fragment-based method. *J. Chem. Phys.* **2016**, *145*, 074102.

(87) Ma, Q.; Werner, H.-J. Explicitly correlated local coupled-cluster methods using pair natural orbitals. *Wiley Interdiscip. Rev. Comput. Mol. Sci* **2018**, *8*, e1371.

(88) Ricke, N.; Welborn, M.; Ye, H.-Z.; Van Voorhis, T. Performance of Bootstrap Embedding for long-range interactions and 2D systems. *Mol. Phys.* **2017**, *115*, 2242–2253.

(89) Ye, H.-Z.; Ricke, N. D.; Tran, H. K.; Van Voorhis, T. Bootstrap Embedding for Molecules. *J. Chem. Theory Comput.* **2019**, *15*, 4497–4506.

(90) Ye, H.-Z.; Van Voorhis, T. Atom-Based Bootstrap Embedding For Molecules. *J. Phys. Chem. Lett.* **2019**, *10*, 6368–6374.

(91) Møller, C.; Plesset, M. S. Note on an Approximation Treatment for Many-Electron Systems. *Phys. Rev.* **1934**, *46*, 618–622.

(92) III, G. D. P.; Bartlett, R. J. A full coupled-cluster singles and doubles model: The inclusion of disconnected triples. *J. Chem. Phys.* **1982**, *76*, 1910–1918.

(93) Ahlrichs, R.; Scharf, P. In *Advances in Chemical Physics: Ab Initio Methods in Quantum Chemistry*; Lawley, K. P., Ed.; John Wiley & Sons, Inc.: Hoboken, NJ, USA, 1987; Vol. 67.

(94) Tsuchimochi, T.; Welborn, M.; Van Voorhis, T. Density matrix embedding in an antisymmetrized geminal power bath. *J. Chem. Phys.* **2015**, *143*, 024107.

(95) Eichkorn, K.; Treutler, O.; Öhm, H.; Häser, M.; Ahlrichs, R. Auxiliary basis sets to approximate Coulomb potentials. *Chem. Phys. Lett.* **1995**, *240*, 283 – 290.

(96) Eichkorn, K.; Weigend, F.; Treutler, O.; Ahlrichs, R. Auxiliary basis sets for main row atoms and transition metals and their use to approximate Coulomb potentials. *Theor. Chim. Acta* **1997**, *97*, 119–124.

(97) Weigend, F. Accurate Coulomb-fitting basis sets for H to Rn. **2006**, *8*, 1057–1065.

(98) Weigend, F. A fully direct RI-HF algorithm: Implementation, optimised auxiliary basis sets, demonstration of accuracy and efficiency. **2002**, *4*, 4285–4291.

(99) Häser, M.; Ahlrichs, R. Improvements on the direct SCF method. *J. Comput. Chem.* **1989**, *10*, 104–111.

(100) Strout, D. L.; Scuseria, G. E. A quantitative study of the scaling properties of the Hartree-Fock method. *J. Chem. Phys.* **1995**, *102*, 8448–8452.

(101) Lambrecht, D. S.; Doser, B.; Ochsenfeld, C. Rigorous integral screening for electron correlation methods. *J. Chem. Phys.* **2005**, *123*, 184102.

(102) Whitten, J. L. Coulombic potential energy integrals and approximations. *J. Chem. Phys.* **1973**, *58*, 4496–4501.

(103) Schütz, M.; Manby, F. R. Linear scaling local coupled cluster theory with density fitting. Part I: 4-external integrals. **2003**, *5*, 3349–3358.

(104) Tew, D. P. Communication: Quasi-robust local density fitting. *J. Chem. Phys.* **2018**, *148*, 011102.

(105) Press, W.; Vetterling, W. *Numerical Recipes in C: The Art of Scientific Computing*; Cambridge University Press, 1992.

(106) McWeeny, R. *Methods of Molecular Quantum Mechanics*; Academic Press: San Diego, California, 1978.

(107) Helgaker, T.; Jørgensen, P.; Olsen, J. *Molecular Electronic Structure Theory*; John Wiley & Sons, LTD: Chichester, 2000.

(108) Rice, J.; Amos, R. On the efficient evaluation of analytic energy gradients. *Chem. Phys. Lett.* **1985**, *122*, 585 – 590.

(109) Gauss, J.; Stanton, J. F. Analytic gradients for the coupled-cluster singles, doubles, and triples (CCSDT) model. *J. Chem. Phys.* **2002**, *116*, 1773–1782.

(110) Koch, H.; Jensen, H. J. A.; Jørgensen, P.; Helgaker, T.; Scuseria, G. E.; Schaefer, H. F. Coupled cluster energy derivatives. Analytic Hessian for the closed-shell coupled cluster singles and doubles wave function: Theory and applications. *J. Chem. Phys.* **1990**, *92*, 4924–4940.

(111) Ye, H.-Z. Frankenstein: An Electronic Structure Method Development Platform. `https://github.com/hongzhouye/frankenstein`, 2020.

(112) Valeev, E. F. Libint: A library for the evaluation of molecular integrals of many-body operators over Gaussian functions. `http://libint.valeyev.net`, 2018.

(113) Sun, Q.; Berkelbach, T. C.; Blunt, N. S.; Booth, G. H.; Guo, S.; Li, Z.; Liu, J.; McClain, J. D.; Sayfutyarova, E. R.; Sharma, S.; Wouters, S.; Chan, G. K. PySCF: the Python-based simulations of chemistry framework. 2017.

(114) Hehre, W. J.; Stewart, R. F.; Pople, J. A. Self-Consistent Molecular-Orbital Methods. I. Use of Gaussian Expansions of Slater-Type Atomic Orbitals. *J. Chem. Phys.* **1969**, *51*, 2657–2664.

(115) Hättig, C. Optimization of auxiliary basis sets for RI-MP2 and RI-CC2 calculations: Core-valence and quintuple-ζ basis sets for H to Ar and QZVPP basis sets for Li to Kr. **2005**, *7*, 59–66.

(116) Boys, S. F. Construction of Some Molecular Orbitals to Be Approximately Invariant for Changes from One Molecule to Another. *Rev. Mod. Phys.* **1960**, *32*, 296–299.

(117) Høyvik, I.-M.; Jansik, B.; Jørgensen, P. Pipek-Mezey localization of occupied and virtual orbitals. *J. Comput. Chem.* **2013**, *34*, 1456–1462.

(118) Knizia, G. Intrinsic Atomic Orbitals: An Unbiased Bridge between Quantum Theory and Chemical Concepts. *J. Chem. Theory Comput.* **2013**, *9*, 4834–4843.

(119) Neese, F. The ORCA program system. *Wiley Interdiscip. Rev. Comput. Mol. Sci* **2012**, *2*, 73–78.

(120) Scuseria, G. E. Ab Initio Calculations of Fullerenes. *Science* **1996**, *271*, 942–945.

(121) Andreoni, W. Computational Approach to the Physical Chemistry of Fullerenes and Their Derivatives. *Ann. Rev. Phys. Chem.* **1998**, *49*, 405–439.

(122) Zheng, G.; Irle, S.; Morokuma, K. Performance of the DFTB method in comparison to DFT and semiempirical methods for geometries and energies of C20-C86 fullerene isomers. *Chem. Phys. Lett.* **2005**, *412*, 210 – 216.

(123) Candian, A.; Gomes Rachid, M.; MacIsaac, H.; Staroverov, V. N.; Peeters, E.; Cami, J. Searching for stable fullerenes in space with computational chemistry. *Mon. Not. R. Astron. Soc* **2019**, *485*, 1137–1146.

(124) Calaminici, P.; Geudtner, G.; Köster, A. M. First-Principle Calculations of Large Fullerenes. *J. Chem. Theory Comput.* **2009**, *5*, 29–32.

(125) Schwerdtfeger, P.; Wirz, L.; Avery, J. Program Fullerene: A software package for constructing and analyzing structures of regular fullerenes. *J. Comput. Chem.* **2013**, *34*, 1508–1526.

(126) Jiménez-Hoyos, C. A.; Rodríguez-Guzmán, R.; Scuseria, G. E. Polyradical Character and Spin Frustration in Fullerene Molecules: An *Ab Initio* Non-Collinear Hartree-Fock Study. **2014**, *118*, 9925–9940.

(127) Lee, J.; Head-Gordon, M. Distinguishing artificial and essential symmetry breaking in a single determinant: approach and application to the C60, C36, and C20 fullerenes. **2019**, *21*, 4763–4778.

(128) Edmiston, C.; Ruedenberg, K. Localized Atomic and Molecular Orbitals. *Rev. Mod. Phys.* **1963**, *35*, 457–464.

(129) Pipek, J.; Mezey, P. G. A fast intrinsic localization procedure applicable for ab initio and semiempirical linear combination of atomic orbital wave functions. *J. Chem. Phys.* **1989**, *90*, 4916–4926.

(130) Boughton, J. W.; Pulay, P. Comparison of the boys and Pipek-Mezey localizations in the local correlation approach and automatic virtual basis selection. *J. Comput. Chem.* **1993**, *14*, 736–740.

(131) Werner, H.-J.; Köppl, C.; Ma, Q.; Schwilk, M. *Fragmentation*; John Wiley & Sons, Ltd, 2017; Chapter 1, pp 1–79.